letters to nature

sufficiently large to ensure that an 80 p.p.m. decrease in glacial atmospheric CO_2 can still be attained even after including the counteracting effects of terrestrial biomass changes and salinity-driven solubility effects[23]. Toggweiler[29] recently developed a model that similarly invokes a reduction in deep-water ventilation to explain the low glacial CO_2 levels. Whereas he generates reduced ventilation by decreasing the vertical exchange between deep and Antarctic surface waters, we suggest that reduced ventilation was driven by limitations to air–sea gas exchange imposed by increased sea ice in this region. □

1. Petit, J. R. et al. Climate and atmospheric history of the past 420,000 years from the Vostok ice core, Antarctica. Nature 399, 429–436 (1999).
2. Sarmiento, J. L. & Toggweiler, J. R. A new model for the role of the oceans in determining atmospheric pCO₂. Nature 308, 621–624 (1984).
3. Siegenthaler, U. & Wenk, T. Rapid atmospheric CO₂ variations and ocean circulation. Nature 308, 624–626 (1984).
4. Knox, F. & McElroy, M. B. Changes in atmospheric CO₂: Influence of the marine biota at high latitude. J. Geophys. Res. 89, 4629–4637 (1984).
5. Martin, J. H. Glacial–interglacial CO₂ change: The iron hypothesis. Paleoceanography 5, 1–13 (1990).
6. Broecker, W. S. & Henderson, G. M. The sequence of events surrounding Termination II and their implications for the cause of glacial–interglacial CO₂ changes. Paleoceanography 13, 352–364 (1998).
7. Opdyke, B. N. & Walker, J. C. G. Return of the coral reef hypothesis: Basin to shelf partitioning of CaCO₃ and its effect on atmospheric CO₂. Geology 20, 733–736 (1982).
8. Boyle, E. A. The role of vertical chemical fractionation in controlling Late Quaternary atmospheric carbon dioxide. J. Geophys. Res. 93, 15701–15714 (1988).
9. Archer, D. & Maier–Reimer, E. Effect of deep-sea sedimentary calcite preservation on atmospheric CO₂ concentration. Nature 367, 260–263 (1994).
10. Toggweiler, J. R. & Samuels, B. in The Global Carbon Cycle (ed. Heimann, M.) 333–366 (Springer, Berlin, 1993).
11. Gnanadesikan, A. & Toggweiler, J. R. Constraints placed by silicon cycling on vertical exchange in general circulation models. Geophys. Res. Lett. 26, 1865–1868 (1999).
12. Charles, C. D. & Fairbanks, R. G. in Geological History of the Polar Oceans: Arctic Versus Antarctic (eds Bleil, U. & Thiede, J.) 519–538 (Kluwer Academic, Dordrecht, 1990).
13. Boyle, E. A. Cadmium and δ¹³C paleochemical ocean distributions during the Stage 2 glacial maximum. Annu. Rev. Earth Planet. Sci. 20, 245–287 (1992).
14. Toggweiler, J. R. & Sarmiento, J. L. in The Carbon Cycle and Atmospheric CO₂: Natural Variations Archean to Present (eds Sundquist, E. T. & Broecker, W. S.) 163–184 (American Geophysical Union, Washington DC, 1985).
15. Marino, B. M., McElroy, M. B., Salawitch, R. J. & Spaulding, W. G. Glacial-to-interglacial variations in the carbon isotopic composition of atmospheric CO₂. Nature 357, 461–466 (1992).
16. Robbins, P. E. & Toole, J. M. The dissolved silica budget as a constraint on the meridional overturning circulation of the Indian Ocean. Deep-Sea Res. 44, 879–906 (1997).
17. Broecker, W. S. et al. How much deep water is formed in the Southern Ocean? J. Geophys. Res. 103, 15833–15843 (1998).
18. Tomczak, M. & Godfrey, J. S. Regional Oceanography: An Introduction 67–87 (Pergamon, Oxford, 1994).
19. Molinelli, E. J. The Antarctic influence on Antarctic Intermediate Water. J. Mar. Res. 39, 267–293 (1981).
20. McCartney, M. S. in A Voyage of Discovery (ed. Angel, M.) 103–119 (Pergamon, Oxford, 1977).
21. Berger, W. H. Deep-sea carbonate and the deglaciation preservation spike in pteropods and foraminifera. Nature 269, 301–304 (1977).
22. Broecker, W. S. An oceanographic explanation for the apparent carbon isotope–cadmium discordancy in the glacial Antarctic? Paleoceanography 8, 137–139 (1993).
23. Broecker, W. S. & Peng, T.-H. Greenhouse Puzzles 2nd edn (Eldigio, Palisades, New York, 1998).
24. Guilderson, T. P., Fairbanks, R. G. & Rubinstone, J. L. Tropical temperature variations since 20,000 years ago: Modulating interhemispheric climate change. Science 263, 663–665 (1994).
25. Smith, H. J., Fischer, H., Wahlen, M., Mastroianni, D. & Deck, B. Dual modes of the carbon cycle since the Last Glacial Maximum. Nature 400, 248–250 (1999).
26. Cooke, D. W. & Hays, J. D. in Antarctic Geoscience: Symposium on Antarctic Geology and Geophysics (ed. Craddock, C.) 1017–1025 (University of Wisconsin Press, Madison, Wisconsin, 1982).
27. Crosta, X., Pichon, J.-J. & Burckle, L. H. Reappraisal of Antarctic seasonal sea-ice at the Last Glacial Maximum. Geophys. Res. Lett. 26, 1865–1868 (1999).
28. François, R. et al. Contribution of Southern Ocean surface-water stratification to low atmospheric CO₂ concentrations during the last glacial period. Nature 389, 929–935 (1997).
29. Toggweiler, J. R. Variation of atmospheric CO₂ by ventilation of the ocean's deepest water. Paleoceanography 14, 571–588 (1999).
30. Broecker, W. S., Takahashi, T. & Takahashi, T. Sources and flow patterns of deep-ocean waters as deduced from potential temperature, salinity, and initial phosphate concentration. J. Geophys. Res. 90, 6925–6939 (1985).

....

Interferometric radar measurements of water level changes on the Amazon flood plain

Douglas E. Alsdorf*, John M. Melack*†, Thomas Dunne†, Leal A. K. Mertes*‡, Laura L. Hess* & Laurence C. Smith§

* Institute for Computational Earth System Science, University of California, Santa Barbara, California 93106, USA
† Donald Bren School of Environmental Science and Management, University of California, Santa Barbara, California 93106, USA
‡ Department of Geography, University of California, Santa Barbara, California 93106, USA
§ Department of Geography, University of California, Los Angeles, California 90095, USA

....

Measurements of water levels in the main channels of rivers, upland tributaries and floodplain lakes are necessary for understanding flooding hazards, methane production, sediment transport and nutrient exchange. But most remote river basins have only a few gauging stations and these tend to be restricted to large river channels. Although radar remote sensing techniques using interferometric phase measurements have the potential to greatly improve spatial sampling, the phase is temporally incoherent over open water and has therefore not been used to determine water levels. Here we use interferometric synthetic aperture radar (SAR) data[1–3], acquired over the central Amazon by the Space Shuttle imaging radar mission[4], to measure subtle water level changes in an area of flooded vegetation on the Amazon flood plain. The technique makes use of the fact that flooded forests and floodplain lakes with emergent shrubs permit radar double-bounce returns from water and vegetation surfaces[5,6], thus allowing coherence to be maintained. Our interferometric phase observations show decreases in water levels of 7–11 cm per day for tributaries and lakes within ~20 km of a main channel and 2–5 cm per day at distances of ~80 km. Proximal floodplain observations are in close agreement with main-channel gauge records, indicating a rapid response of the flood plain to decreases in river stage. With additional data from future satellite missions, the technique described here should provide direct observations important for understanding flood dynamics and hydrologic exchange between rivers and flood plains.

Climatically driven, seasonal changes in river water levels (river stages) govern a wide range of hydrologic, geomorphological and ecological processes. Hydrologic modelling of the Amazon flood wave predicts discharge only along the main channel (the main stem), and suggests that up to 30% of mainstem flow exchanges with the flood plain[7]. On the basis of transport models, the annual sediment exchange between the main channel and flood plain is more than twice the flux through the most downstream river gauge at Obidos[8]. However, the models do not describe the sources or residence times of the floodplain water; these are key variables for measuring biological productivity and sedimentation. For example, observations of a small local catchment demonstrate that early in the water year, the lake contains nearly 70% river water whereas later in the water year, local runoff and other sources increase lake stage, preventing rising flood-stage river water from entering and exchanging with the lake[9]. Because very few of the ~8,000 Amazon floodplain lakes are gauged, the generality of these observations is unclear[10].

Remotely sensed observations of the water surface provide an alternative to permanent gauging. Satellite radar altimetry promises a stage elevation accuracy of about 10 cm: but because altimetry is a profiling and not an imaging technique, it is applicable only to water
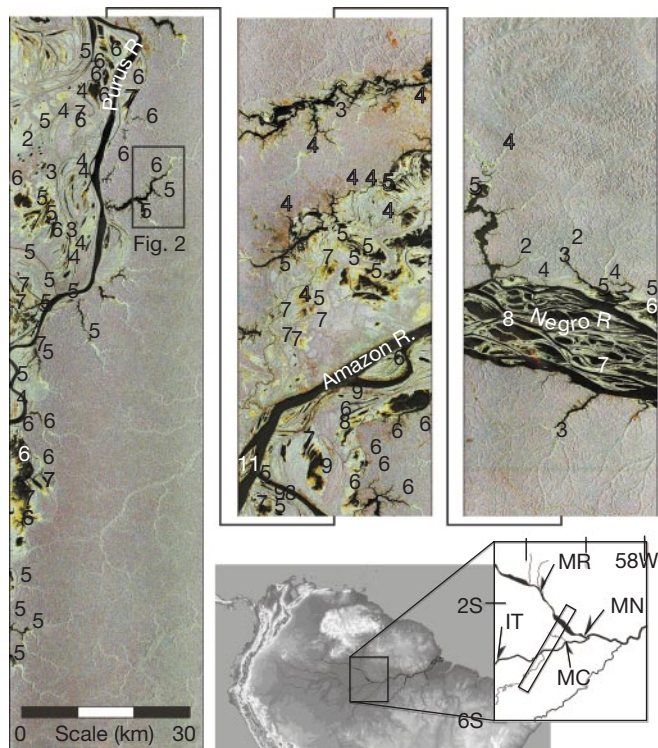
Figure 1 SIR-C swath and location map. Topographic map and close-up at lower right indicate the swath location (rectangle) relative to the surrounding gauging stations (MN, Manaus; MC, Manacapuru; IT, Itapeua; MR, Moura). The Solimões–Amazon River stretches from IT to MN and eastward, the Negro River extends from MN to MR and westward, and the Purus River joins the Solimões–Amazon in the southern half of the SIR-C swath. (2S and 6S indicate 2° and 6° S, 58W indicates 58° W.) The southern end of the 350-km-long SIR-C amplitude composite is the leftmost panel while the northern end is the rightmost panel. In the amplitude image, SIR-C C-band HH-polarization intensities are coloured red, L-HH are green, and L-HV are blue, thus yellows and greens within tributaries and floodplain lakes indicate strong, double-bounce L-HH returns marking inundated vegetation. Interferometrically determined local stage decreases in centimetres, from 9 to 10 October 1994, are noted by single-digit numbers, except the 11 cm drop near the confluence of the Purus with the Amazon river. For clarity, only half of the ~200 observed drops are noted. The amplitude composite is in SAR coordinates; thus the scale bar is approximate.

bodies greater than about two kilometres in width (its height accuracy is limited by orbital, range, and atmospheric errors[11,12]). Imagery from space-borne platforms, such as passive microwave sensors, synthetic aperture radars and the Landsat thematic mapper, have been used to map the extent and timing of inundation[5,13–16], yet these methods do not directly measure stage elevation or change. Here we report that interferometric processing of SAR data from the SIR-C mission[4] yields centimetre-scale measurements of stage change in floodplain lakes, floodplain channels (*paranas*), and upland tributaries (*igarapes*).

Radar backscatter intensity data from the second phase of the SIR-C mission were collected over the Amazon basin in October 1994, at X- (3.1 cm), C- (5.7 cm), and L-band (24.0 cm) wavelengths, and with horizontal and vertical polarizations. (By convention, for example, L-HV indicates a horizontally-sent vertically-received L-band radar pulse). Radar echoes at X- and C-band wavelengths backscatter from the tops of most forest canopies, while L-band echoes penetrate to the underlying ground or water surface: thus composite images from these simultaneously acquired radar echoes can be used to delineate vegetation types and floodplain inundation[5] (Figs 1 and 2). Relative to nonflooded forests, increased backscatter intensities at L-HH are observed over flooded

forests, while compared to open water, C-HH backscattering increases over floating aquatic macrophytes and emergent shrubs in floodplain lakes. These flooded environments usually produce a two-bounce travel path of the radar pulse that includes interactions between the water surface and trunks of vegetation. Conversely, low backscattering is observed at both L and C bands over open water[5]. For example, the lake shown in Fig. 2 connects directly to the Purus River, a major tributary of the Solimões–Amazon River. Small tributaries drain the surrounding forested upland (for example, along profile B) and flood forests near their confluence with the lake (for example, along profile A).

Centimetre-scale topographic displacements resulting from earthquakes, inter-seismic strain accumulation, and flowing glaciers have been accurately measured using interferometric processing of SAR phase data[1–3,17–21]. The processing method requires two SAR image acquisitions from identical (or nearly identical) viewing geometries before and after the displacement phenomenon; co-registration of the two images to a sub-pixel accuracy; and subtraction of the complex phase and amplitude values at each SAR image pixel. The value of the resulting interferometric phase at each pixel varies between $-\pi$ and $+\pi$, and is primarily a function of the distance between the radar antenna positions during acquisition (that is, the Shuttle baseline), topographic relief, topographic displacement, and the degree of correlation between the individual scattering elements that comprise each pixel location (that is, coherence[22,23]). As expected for C-band wavelengths[24–27], the scattering elements of the tree canopy (that is, leaves and branches easily moved by gentle breezes) completely decorrelated in the 24 hours between SIR-C acquisitions, whereas at L-band, the elements were typically comprised of earth and immobile trunks of vegetation which enabled strong phase-correlation (see profiles in Fig. 2).

The most unexpected result of the interferometric processing is the strong, L-band coherence (>0.5) maintained over regions marked by flooded forest and floodplain lakes with tree canopies and emergent shrubs (profiles shown in Fig. 2). Radar pulse interactions with open water are specular (that is, reflect away from the antenna); thus L-band coherence over open rivers and lakes was low, averaging 0.26. However, the strong coherence of tributaries within flooded forests and of floodplain lakes with vegetation enabled interferometric phase measurements of the earth, vegetation trunks, and water surfaces that returned the radar echoes. In these environments, the higher-amplitude L-HH returns compared to L-HV[5] produced stronger correlation, thus leading to more reliable interferometric phase measurements.

The observed interferometric phase measured both the local topography and also any surface displacements that occurred during the 24 hours separating the two SIR-C acquisitions. To separate these components, either a synthetic interferogram based on a digital elevation model (DEM) or additional SAR interferograms free of displacement phenomena can be subtracted from the observed phase[3]. Unfortunately, neither a high-resolution DEM nor a third SAR acquisition were available. Instead, the short, 9–10 October Shuttle baseline (perpendicular component of only 63 m) enables discrimination of the topographic and displacement components of the total measured phase. Using this baseline, the amount of topographic relief measured from $-\pi$ to $+\pi$ at the L-band wavelength is 275 m (refs 24, 25). Since the relief throughout the study area is known to be less than ~65 m, only ~1/4 of a cycle ($\sim 1/2\pi$ or less) of the observed interferometric phase can be attributed to topography. Indeed, for the imaged floodplain and upland areas, phase values of only 0.0 to -0.5 radians (blue pixels in Fig. 2) are found in the interferogram, indicating low regional relief.

Although the short baseline prohibits accurate measurements of Amazon basin topography[27], its orientation enables simple physiographic comparisons. For example, the phase values in profile B of Fig. 2 reach peak values where crossing an upstream valley (given the SIR-C baseline orientation, phase peaks are expected over topographic
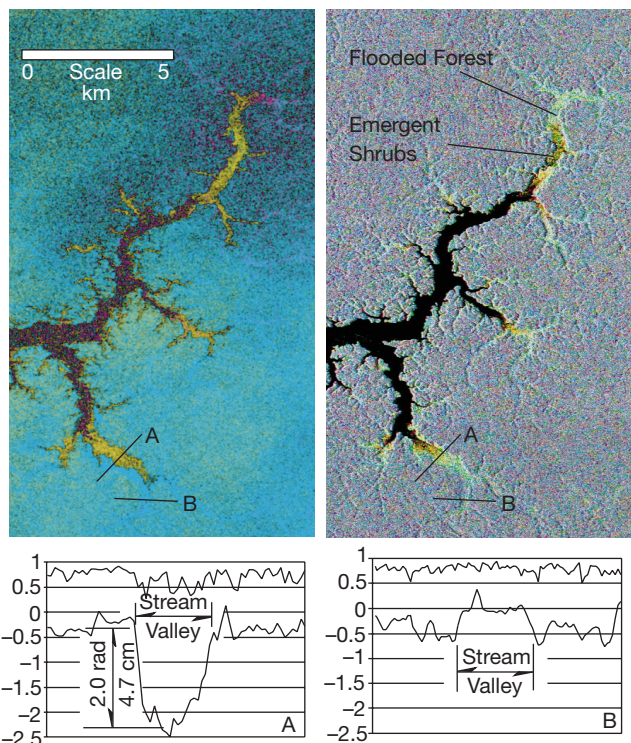
Figure 2 SIR-C L-HH flattened interferogram (left) and amplitude composite (right). See Fig. 1 for location of this area along the Purus River, a tributary of the Amazon–Solimões River. A and B mark profiles of interferometric phase (bottom line in both profiles; in this case, units on vertical axes are radians) and corresponding interferometric coherence (top line in both profiles; in this case, units are interferometric correlation). Using the red–green–blue colour scheme of Fig. 1 on the amplitude composite, flooded forests in the upper tributary reaches are bright yellow and green while open water is black. Tributaries marked by mottled-greenish pixels indicate emergent shrubs. Flooded forests and emergent shrubs are marked by coherent interferometric phase values of about −2.5 radians (yellow pixels in the interferogram). Phase image brightness is a function of the local L-HH backscatter intensity.

valleys). Yet, unexpectedly, the phase values along profile A reach their lowest values where crossing the same valley further downstream. This difference cannot be ascribed to poor correlation (correlation values for both plots are almost all greater than 0.5) nor to a topographic ridge (the phase trough is ~4 times greater in A than the phase peak in B, thus any possible topographic ridge would encompass ~4 times the relief of the valley—the amplitude image does not show such a ridge). Phase differences related to atmospheric water vapour can also be discounted because they are usually longer in wavelength and spatially distinct from phase signatures related to tributaries and floodplain lakes. Therefore, the phase trough must indicate a surface displacement away from the Shuttle. Given the spatial distribution of the phase trough, a decrease in the elevation of the water surface that occurred during the 24 hours separating the two SIR-C acquisitions is the most likely displacement phenomenon. As the water surface elevation change is purely vertical, the 2.0-radian trough can be projected from the SAR line-of-sight direction to yield a stage decrease of nearly 5 cm ($\Delta z = \lambda\varphi/[4\pi\cos(\text{look angle})]$, where $\lambda = 24.0$ cm, φ is the displacement phase, the look angle is 35.2°, and Δz is the vertical displacement).

Using the method described above, the change in stage for vegetation-covered floodplain lakes and tributaries in flooded forests was measured throughout the SIR-C interferometric swath (Fig. 1). Drainage path distances were measured from each water body to the closest mainstem river, that is, the Solimões–Amazon, Negro or Purus rivers. The largest drops of 7–11 cm were measured

in floodplain water bodies within ~20 km of either the Solimões–Amazon or Purus Rivers or within the Negro archipelago. For comparison, the Manaus gauge (Fig. 1) recorded a drop of 12 cm in water level from 9 to 10 October 1994, and an average daily decrease of 12 cm in the previous 7 days. The Manacapuru, Itapeua and Moura gauges (Fig. 1) recorded decreases of 7, 5 and 6 cm, respectively, while averages over the previous 7 days were 11, 7 and 11 cm, respectively.

Interferometric measurements of decreasing floodplain water levels indicate that the proximal flood plain was rapidly evacuating water to mainstem channels during the SIR-C acquisitions, in response to the 11 cm drop in channel stage. At distances greater than ~30 km, where the flood plain includes input from surrounding upland tributaries and lakes, drops were 2–6 cm. Although these distal water bodies ultimately discharge to a mainstem river, it is likely that many days are necessary for exchange. Consecutive daily decreases of mainstem water levels since early July 1994 may have worked to decrease distal water levels while local catchment inputs (precipitation, groundwater flow and runoff) worked to increase water levels. For comparison, tributaries and lakes in upland areas that drain directly to the Solimões–Amazon or Purus Rivers also had interferometrically measured drops of 2–6 cm, with the largest drops occurring within 20 km of either mainstem river. Viewed collectively, the dominant trend in the SIR-C observations is that drops in water level diminish with increasing distance from a mainstem river. Proximal floodplain waters are quickly evacuated to mainstem rivers in response to decreased river discharge, even in low-lying areas of the Amazon. This indicates the importance and rapidity of hydrologic transfer from flood plain to river channel during recessional flow.

These observations from the SIR-C mission provide, we believe for the first time, a spatial image of centimetre-scale variations in floodplain water level response to changing river discharge; they imply that future satellite L-HH band SAR missions are capable of yielding interferometric measurements of stage change over the entire Amazon flood plain. Furthermore, our observations show that planning and acquiring L-HH interferometric radar data over other large river systems—such as the Congo of central Africa and smaller systems such as the Alligator rivers near Darwin, Australia—should yield spatial and temporal measurements of stage changes where vegetation characteristics permit interferometric correlation to be maintained. Thus, with a broader application to global wetlands, our work suggests that the complex dynamics of floods, including the timing and rates of hydrologic exchange between channels and flood plains, can be remotely measured with greatly improved resolution. □

1. Goldstein, R. M., Engelhardt, H., Kamb, B. & Frolich, R. M. Satellite radar interferometry for monitoring ice sheet motion: Application to an Antarctic ice stream. *Science* **262**, 1525–1530 (1993).
2. Massonnet, D. *et al.* The displacement field of the Landers earthquake mapped by radar interferometry. *Nature* **364**, 138–142 (1993).
3. Zebker, H. A., Rosen, P. A., Goldstein, R. M., Gabriel, A. & Werner, C. L. On the derivation of coseismic displacement fields using differential radar interferometry: The Landers earthquake. *J. Geophys. Res.* **99**, 19617–19634 (1994).
4. Stofan, E. R., *et al.* Overview of results of Spaceborne Imaging Radar-C, X-band synthetic aperture radar (SIR-C/X-SAR). *IEEE Trans. Geosci. Remote Sensing* **33**, 817–828 (1995).
5. Hess, L. L., Melack, J. M., Filoso, S. & Wang, Y. Delineation of inundated area and vegetation along the Amazon floodplain with SIR-C synthetic aperture radar. *IEEE Trans. Geosci. Remote Sensing* **33**, 896–904 (1995).
6. Wang, Y., Hess, L. L., Filoso, S. & Melack, J. M. Understanding the radar backscattering from flooded and nonflooded Amazonian forests: Results from canopy backscatter modeling. *Remote Sensing Environ.* **54**, 324–332 (1995).
7. Richey, J. E. *et al.* Sources and routing of the Amazon river flood wave. *Glob. Biogeochem. Cycles* **3**, 191–204 (1989).
8. Dunne, T., Mertes, L. A. K., Meade, R. H., Richey, J. E. & Forsberg, B. R. Exchanges of sediment between the flood plain and channel of the Amazon River in Brazil. *GSA Bull.* **110**, 450–467 (1998).
9. Lesack, L. F. W. & Melack, J. M. Flooding hydrology and mixture dynamics of lake water derived from multiple sources in an Amazon floodplain lake. *Wat. Resour. Res.* **31**, 329–345 (1995).
10. Melack, J. M. & Forsberg, B. R. in *The Biogeochemistry of the Amazon Basin and its Role in a Changing World* (eds McClain, M. E., Victoria, R. L. Richey, J. E.) (Oxford Univ. Press, New York, in the press).
11. Birkett, C. M. The contribution of TOPEX/POSEIDON to the global monitoring of climatically

176 NATURE | VOL 404 | 9 MARCH 2000 | www.nature.com

sensitive lakes. *J. Geophys. Res.* **100**, 25179–25204 (1995).

12. Birkett, C. M. Contribution of the TOPEX NASA radar altimeter to the global monitoring of large rivers and wetlands. *Wat. Resour. Res.* **34**, 1223–1239 (1998).

13. Mertes, L. A. K. Documentation and significance of the perirheic zone on inundated floodplains. *Wat. Resour. Res.* **33**, 1749–1762 (1997).

14. Smith, L. C. Satellite remote sensing of river inundation area, stage, and discharge: A review. *Hydrol. Processes* **11**, 1427–1439 (1997).

15. Mertes, L. A. K. *et al.* Spatial patterns of hydrology, geomorphology, and vegetation on the floodplain of the Amazon River in Brazil from a remote sensing perspective. *Geomorphology* **13**, 215–232 (1995).

16. Sippel, S. J., Hamilton, S. K., Melack, J. M. & Novo, E. M. M. Passive microwave observations of inundation area and the area/stage relation in the Amazon River floodplain. *Int. J. Remote Sensing* **19**, 3055–3074 (1998).

17. Peltzer, G. & Rosen, P. Surface displacement of the 17 May 1993 Eureka Valley, California, earthquake observed by SAR interferometry. *Science* **268**, 1333–1336 (1995).

18. Wicks, C., Thatcher, W. & Dzurisin, D. Migration of fluids beneath Yellowstone caldera inferred from satellite radar interferometry. *Science* **282**, 458–462 (1998).

19. Burgmann, R., Fielding, E. & Sukhatme, J. Slip along the Hayward fault, California, estimated from space-based synthetic aperture radar interferometry. *Geology* **26**, 559–562 (1998).

20. Rignot, E. J., Gogineni, S. P., Krabill, W. B. & Ekholm, S. North and northeast Greenland ice discharge from satellite radar inteferometry. *Science* **272**, 934–937 (1997).

21. Joughin, I., Kwok, R. & Fahnestock, M. Estimation of ice-sheet motion using satellite radar interferometry: Method and error analysis with application to Humboldt Glacier, Greenland. *J. Glaciol.* **42**, 564–575 (1996).

22. Li, F. K. & Goldstein, R. M. Studies of multibaseline spaceborne interferometric synthetic aperture radars. *IEEE Trans. Geosci. Remote Sensing* **28**, 88–97 (1990).

23. Zebker, H. A. & Villasenor, J. Decorrelation in interferometric radar echoes. *IEEE Trans. Geosci. Remote Sensing* **30**, 950–959 (1992).

24. Rosen, P. A., Hensley, S., Zebker, H. A., Webb, F. H. & Fielding, E. J. Surface deformation and coherence measurements of Kilauea Volcano, Hawaii, from SIR-C radar interferometry. *J. Geophys. Res.* **101**, 23109–23125 (1996).

25. Massonnet, D. & Rabaute, T. Radar interferometry: Limits and potential. *IEEE Trans. Geosci. Remote Sensing* **31**, 455–464 (1993).

26. Zebker, H. A., Rosen, P. A., Hensley, S. & Mouginis-Mark, P. J. Analysis of active lava flows on Kilauea volcano, Hawaii, using SIR-C radar correlation measurements. *Geology* **24**, 495–498 (1996).

27. Rignot, E. Dual-frequency interferometric SAR observations of a tropical rain-forest. *Geophys. Res. Lett.* **23**, 993–996 (1996).

···

Delayed biological recovery from extinctions throughout the fossil record

James W. Kirchner* & **Anne Weil**†

* *Department of Geology and Geophysics, University of California, Berkeley, California, 94720-4767, USA*
† *Department of Biological Anthropology and Anatomy, Duke University, Durham, North Carolina 27708-0383, USA*

···

How quickly does biodiversity rebound after extinctions? Palaeobiologists have examined the temporal, taxonomic and geographic patterns of recovery following individual mass extinctions in detail[1–5], but have not analysed recoveries from extinctions throughout the fossil record as a whole. Here, we measure how fast biodiversity rebounds after extinctions in general, rather than after individual mass extinctions, by calculating the cross-correlation between extinction and origination rates across the entire Phanerozoic marine fossil record. Our results show that extinction rates are not significantly correlated with contemporaneous origination rates, but instead are correlated with origination rates roughly 10 million years later. This lagged correlation persists when we remove the 'Big Five' major mass extinctions, indicating that recovery times following mass

extinctions and background extinctions are similar. Our results suggest that there are intrinsic limits to how quickly global biodiversity can recover after extinction events, regardless of their magnitude. They also imply that today's anthropogenic extinctions will diminish biodiversity for millions of years to come.

A key component of biotic recovery is the time lag between episodes of rapid extinction and subsequent periods of rapid origination. Originations rebuild biodiversity, and origination rates are commonly assumed to peak when ecosystems have recovered sufficient diversity to inhibit further diversification[6]. Thus, the elapsed time between extinction rate peaks and origination rate peaks is one measure of the recovery time (Fig. 1). We can estimate the average time lag for the whole fossil record using the cross-correlation between extinctions and originations, which measures how closely the two time series resemble each other, when one is shifted forwards or backwards by a specified interval. For regularly spaced time series, the cross-correlation function could be calculated as

$$r_{EO}(k) = \frac{\Sigma(E_i - \bar{E}_i)(O_j - \bar{O}_j)}{\sqrt{\Sigma(E_i - \bar{E}_i)^2}\sqrt{\Sigma(O_j - \bar{O}_j)^2}}, \quad j = i + k \qquad (1)$$

where E and O are the extinction and origination time series, and $r_{EO}(k)$ is their cross-correlation when originations lag extinctions by k steps. This direct approach cannot be applied to the fossil record, because its stratigraphic boundaries are unevenly spaced in time. Nor should one simply even out the spacing by interpolating within each stratigraphic interval, because this introduces artefactual correlation among the interpolated points[7,8]. Instead, we use equation (1) to calculate the correlation between all pairs of points E_i and O_j whose separations in time, $t_j - t_i$, fall within 5 Myr bins of lag time (rather than points separated by fixed numbers of steps); this yields a geostatistical approximation to the cross-correlation function[9] (Fig. 2a, b). A second approach to calculating the cross-correlation between two unevenly spaced time series is through their Fourier transforms[10,11]:

$$r_{EO}(\tau) = FT^{-1}(FT\{E\}FT^{\star}\{O\}) \qquad (2)$$

where FT, $FT^{\star}$ and FT^{-1} denote the Fourier transform, its complex conjugate and its inverse, respectively, and $r_{EO}(\tau)$ is the cross-correlation between E and O at a lag of τ Myr (Fig. 2c, d). We use the Lomb–Scargle Fourier transform[11–14] to calculate $FT\{E\}$ and $FT^{\star}\{O\}$ directly from the unevenly spaced fossil data, without interpolation. The Lomb–Scargle algorithm has similar statistical properties, when applied to unevenly spaced data, to those of conventional Fourier transform algorithms when applied to evenly spaced data[14].

Our source data are Sepkoski's compilations of fossil marine animal genera[15] and families[16], with revisions through 1997. Because long-term drift could obscure the cross-correlations that we seek to analyse, we subtracted the long-term trends (shown as dotted lines in Fig. 1b, c) from the extinction and origination time series before analysis.

The resulting cross-correlation functions (Fig. 2) show that extinctions and originations are not significantly correlated over short lag periods, indicating that, on average, extinctions do not trigger immediate evolutionary rebounds. Instead, the cross-correlation is strongest when originations lag extinctions by roughly 10 Myr. This indicates that the average interval between extinction peaks and origination peaks, and thus the average recovery time from extinctions, is about 10 Myr across the fossil record. The statistical significance of these cross-correlations—that is, the chance of correlations this strong arising by chance at any lag, from −15 to 35 Myr—is $P < 0.05$ for all but one of the 16 cases shown in Fig. 2 (see Supplementary Information). The peak cross-correlation occurs at similar lags with either calculation method, and in both the genus and family data sets, indicating that this result